

Reaction Mechanism of Hydrogen Generation and Nitrogen Fixation at Carbon Nitride/Double Perovskite Heterojunctions

Costanza Tedesco, Luca Gregori, Angelica Simbula, Federico Pitzalis, Andrea Speltini, Francesca Merlo, Silvia Colella, Andrea Listorti, Edoardo Mosconi,* Asma A. Alothman, Waldemar Kaiser, Michele Saba, Antonella Profumo, Filippo De Angelis, and Lorenzo Malavasi*

Photocatalytically active heterojunctions based on metal halide perovskites (MHPs) are drawing significant interest for their chameleon ability to foster several redox reactions. The lack of mechanistic insights into their performance, however, limits the ability of engineering novel and optimized materials. Herein, a report is made on a composite system including a double perovskite, $\text{Cs}_2\text{AgBiCl}_6/\text{g-C}_3\text{N}_4$, used in parallel for solar-driven hydrogen generation and nitrogen reduction, quantified by a rigorous analytical approach. The composite efficiently promotes the two reactions, but its activity strongly depends on the perovskite/carbon nitride relative amounts. Through advanced spectroscopic investigation and density function theory (DFT) modeling the H_2 and NH_3 production reaction mechanisms are studied, finding perovskite halide vacancies as the primary reactive sites for hydrogen generation together with a positive contribution of low loaded $\text{g-C}_3\text{N}_4$ in reducing carrier recombination. For nitrogen reduction, instead, the active sites are $\text{g-C}_3\text{N}_4$ nitrogen vacancies, and the heterojunction best performs at low perovskites loadings where the composites maximize light absorption and reduce carrier losses. It is believed that these insights are important add-ons toward universal exploitation of MHPs in contemporary photocatalysis.


1. Introduction

Photocatalytic reactions mediated by metal halide perovskites (MHPs) have become a topic of current interest because of the promise of improved low-cost devices for solar fuel production.^[1–8] Thanks to their excellent optoelectronic properties, namely tunable band gap, high absorption coefficient, low exciton binding energy, and high carrier mobility, MHPs were successfully applied to a wide range of photocatalytic reactions. Furthermore, a suitable band alignment of MHPs with the most common redox half-reactions allows to run both reduction and oxidation reactions,^[1] as confirmed by the recent experimental demonstrations of the two most representative examples, namely hydrogen photogeneration and CO_2 reduction.^[1–3,9–16]

With respect to traditional metal oxides photocatalysts, MHPs present a large chemical and structural variety, which allows the design and tailoring of the material composition for the envisaged

C. Tedesco, A. Speltini, F. Merlo, A. Profumo, L. Malavasi
Department of Chemistry and INSTM
University of Pavia
Via Taramelli 16, 27100 Pavia, Italy
E-mail: lorenzo.malavasi@unipv.it

L. Gregori, F. De Angelis
Department of Chemistry
Biology and Biotechnology
University of Perugia and INSTM
Via Elce di Sotto 8, 06123 Perugia, Italy

 The ORCID identification number(s) for the author(s) of this article can be found under <https://doi.org/10.1002/aesr.202400040>.

© 2024 The Authors. Advanced Energy and Sustainability Research published by Wiley-VCH GmbH. This is an open access article under the terms of the Creative Commons Attribution License, which permits use, distribution and reproduction in any medium, provided the original work is properly cited.

DOI: 10.1002/aesr.202400040

A. Simbula, F. Pitzalis, M. Saba
Dipartimento di Fisica
Università di Cagliari
09042 Monserrato, Italy

S. Colella
CNR NANOTEC - c/o Dipartimento di Chimica
Università di Bari
Via Orabona 4, 70126 Bari, Italy

A. Listorti
Department of Chemistry
University of Bari "Aldo Moro"
via Orabona 4, 70126 Bari, Italy

E. Mosconi, W. Kaiser, F. De Angelis
Computational Laboratory for Hybrid/Organic Photovoltaics (CLHYO)
Istituto CNR di Scienze e Tecnologie Chimiche "Giulio Natta" (CNR-SCITEC)
Via Elce di Sotto 8, 06123 Perugia, Italy
E-mail: edoardo@thch.unipg.it

solar-drive reaction. In this respect, both lead-based and lead-free systems have been explored, ranging from 3D to 2D perovskites, perovskite derivatives of general formula $A_3B_2X_9$, and $A_2(BB')X_6$ double perovskites.^[17–27]

The general strategy to realize a spatial separation of photo-excited electron–hole pairs in MHPs-based photocatalysts is to design suitable heterojunctions by coupling two semiconductors.^[28–32] In addition, the second semiconductor can also act as co-catalyst to improve surface reaction.^[33] Again, the high tunability of MHPs allows the design of materials with suitable conduction band (CB) and valence band (VB) offsets to achieve the heterojunction and to provide enough overpotential to drive the target photoreaction.

In recent years, several type II and Z-scheme heterojunctions including MHPs have been reported for a range of photocatalytic reactions. The partner semiconductor of choice, in most cases, has been graphitic carbon nitride ($g\text{-C}_3\text{N}_4$).^[17–19,34–40] $g\text{-C}_3\text{N}_4$ is one of the most appealing and performing metal-free photocatalysts having a good absorption in the visible spectrum (band gap of about 2.7 eV), ease of preparation from cheap precursors, no toxicity, and high stability in both acidic and basic media.^[41] In MHPs/ $g\text{-C}_3\text{N}_4$ heterojunctions, photogenerated electrons tend to migrate and accumulate in $g\text{-C}_3\text{N}_4$, where active sites for the photocatalytic reaction are present, while holes from graphitic carbon nitride migrate to the MHP.^[9,19,37] In contrast, the perovskite itself can efficiently photogenerate hydrogen by hydrohalic acid splitting, as demonstrated in MAPbI_3 (MA=methylammonium) and in other systems such as CsPbBr_3 .^[21,30,42] Moving away from toxic lead, Bi-based perovskite derivatives were also successfully employed in heterojunctions for hydrogen photogeneration.^[19,36,40] More recently, significant interest has been triggered by Bi-based double perovskites for their potential use in different photocatalytic reactions thanks to their superior stability, wide compositional tunability, and good optical properties. $\text{Cs}_2\text{AgBiBr}_6$ has been investigated for photocatalytic CO_2 reduction, where it has been found that the surface of the perovskites acts as reaction site in the reduction process.^[24,38] Fewer reports refer to the hydrogen generation mediated by this double perovskite, with the $\text{NiCoP}/\text{Cs}_2\text{AgBiBr}_6$ heterojunction representing the best report to date with about $400 \mu\text{mol g}^{-1} \text{h}^{-1}$ of evolved hydrogen under 300 W illumination at $\lambda \geq 420 \text{ nm}$.^[43] The proposed mechanism in this system considers an effective transfer of electrons from $\text{Cs}_2\text{AgBiBr}_6$ to the CB of NiCoP on which the H_2 generation reaction occurs.^[43]

While there is an increasing amount of evidence about the effective role of MHPs and MHP-based heterojunctions in running various photocatalytic processes, a detailed description of the reaction mechanism(s) is still lacking. For this reason, herein, we report a combined experimental and computational

study on $\text{Cs}_2\text{AgBiCl}_6/g\text{-C}_3\text{N}_4$ heterojunctions which have been applied to run two different photocatalytic reactions: hydrogen generation and nitrogen reduction to ammonia. To the best of our knowledge, this last reaction has never been explored before in any MHP-based system. $\text{Cs}_2\text{AgBiCl}_6$ has been selected based on its optimal moisture stability, suitable band alignment, and because it is a lead-free compound. The $\text{Cs}_2\text{AgBiCl}_6/g\text{-C}_3\text{N}_4$ composite system has been investigated in the whole weight ratio between perovskite and $g\text{-C}_3\text{N}_4$. We found that MHP-rich compositions perform better in the H_2 photogeneration, while $g\text{-C}_3\text{N}_4$ -rich systems are more effective in the nitrogen photofixation reaction. As reported earlier, due to the limited microscopic details about the photocatalytic activity of MHP-based heterojunctions, key aim of this work is to provide a comprehensive description of the mechanism underpinning the solar-light mediated reactions in terms of charge carrier dynamics and reaction active sites. This has been achieved through a detailed photo-physical and computational modeling study on the prepared systems and for the two photocatalytic reactions investigated, providing solid clues about reaction mechanisms. While the application of MHPs-based heterojunction for hydrogen photogeneration is now quite well established, the present work clarifies the suitability of the present systems to run nitrogen reduction reaction, exploring a new avenue in the photocatalytic application of MHPs.

2. Results and Discussion

The $\text{Cs}_2\text{AgBiCl}_6/g\text{-C}_3\text{N}_4$ system has been synthesized according to the experimental procedure reported in the Experimental Section. Weight ratios investigated between $\text{Cs}_2\text{AgBiCl}_6$ and $g\text{-C}_3\text{N}_4$ nanosheets are (wt% of perovskite) 100, 99, 97.5, 95, 90, 85, 82.5, 80, 70, 50, 25, 10, 2.5, and 0. **Figure 1a** reports the room temperature X-ray diffraction (XRD) patterns of some selected compositions investigated (corresponding to the best performances, see later in the text).

Bottom part of **Figure 1a** shows the pattern of $\text{Cs}_2\text{AgBiCl}_6$ double perovskite (with a sketch of its crystal structure in **Figure 1b**) displaying a cubic symmetry with $Fm\bar{3}m$ space group (#225) and a lattice parameter of 10.7761(2) Å, in agreement with previous results.^[44] **Figure S1a**, Supporting Information, shows a comparison between experimental and calculated patterns for $\text{Cs}_2\text{AgBiCl}_6$. At the top of **Figure 1a**, the X-ray pattern of pure $g\text{-C}_3\text{N}_4$ nanosheets is reported. The typical broad peaks around 13° and 28° corresponding to the (100) and (002) reflections are clearly visible.^[45] The patterns of the composites (cf. **Figure 1b**) are dominated by perovskite reflections at high wt% of $\text{Cs}_2\text{AgBiCl}_6$ and the reflections of $g\text{-C}_3\text{N}_4$ start to be evident around 50 wt%. Also, at 10 wt% of perovskite, its pattern is still clearly detectable, due to its high scattering power with respect to $g\text{-C}_3\text{N}_4$. Morphological inspection of $\text{Cs}_2\text{AgBiCl}_6$, $g\text{-C}_3\text{N}_4$, and selected composites has been carried out by scanning electron microscopy (SEM) and the results are reported in **Figure S2**, Supporting Information. $g\text{-C}_3\text{N}_4$ nanosheets have also been characterized by transmission electron microscopy (TEM) and representative images showing their nanostructure are shown in **Figure S3**, Supporting Information. Finally, elemental mapping through energy-dispersive (EDS) X-ray spectroscopy has been

E. Mosconi, A. A. Allothman
Chemistry Department
College of Science
King Saud University
Riyadh 11451, Kingdom of Saudi Arabia

F. De Angelis
SKKU Institute of Energy Science and Technology (SIEST)
Sungkyunkwan University
Suwon 440-746, Korea

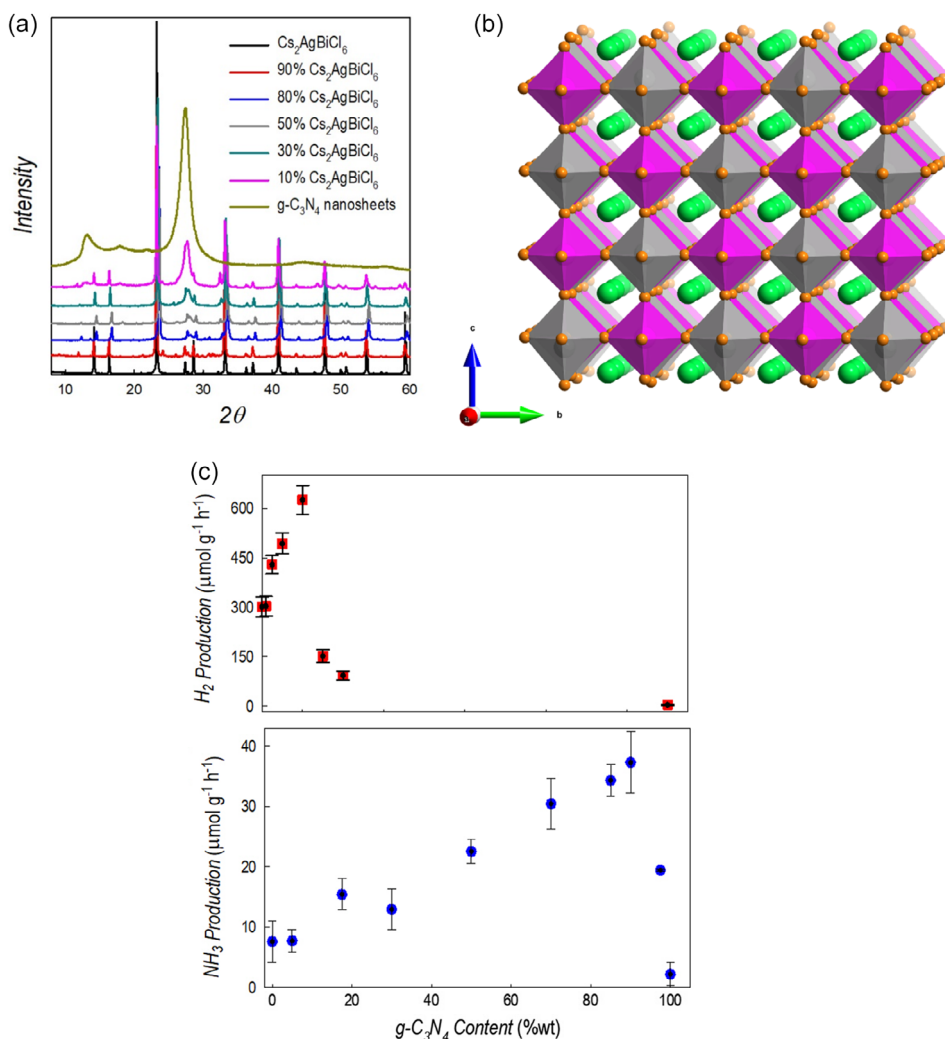


Figure 1. a) XRD pattern of selected Cs₂AgBiCl₆/g-C₃N₄ composites; b) sketch of Cs₂AgBiCl₆ crystal structure where Cs⁺ ions are shown as green spheres, the chloride ions as orange spheres, while the Ag and Bi octahedra are shown as silver and purple polyhedra, respectively; c) hydrogen and ammonia productions as a function of g-C₃N₄ wt% in the composites. ($n = 3$, simulated solar light, 500 W m⁻²).

carried out for the composite with 10 wt% of Cs₂AgBiCl₆, as an illustrative example, and is reported in Figure S4, Supporting Information, further confirming the formation of a composite between the two semiconductors.

Figure 1c reports the results in terms of hydrogen and ammonia evolution rates (top and bottom graphs, respectively), expressed as μmol g⁻¹ h⁻¹, obtained by photocatalytic experiments under simulated solar light (details in the Experimental Section). The two production rates follow opposite trends as a function of composition, with perovskite-rich samples performing better for the hydrogen generation and perovskite-poor compositions running the nitrogen reduction more efficiently. The trend of hydrogen evolution rate (HER), deriving from HCl splitting, steeply increases from pure Cs₂AgBiCl₆ to the composite including 10 wt% of g-C₃N₄, reaching a value of 625 μmol g⁻¹ h⁻¹ which is more than doubled with respect to pure perovskite. Note that pure g-C₃N₄, under these reaction conditions, provides an HER of 4 μmol g⁻¹ h⁻¹. The reported data

confirm a synergistic effect of the composite in enhancing the photocatalytic HCl splitting ability of Cs₂AgBiCl₆, thanks to the formation of an effective heterojunction (see later in the text). The present results, while being the first related to the hydrogen generation by Cs₂AgBiCl₆, can be compared to analogous systems involving double perovskites. To date, only the HBr splitting by Cs₂AgBiBr₆ has been explored in heterojunctions with reduced graphene oxide, NiCoP or nitrogen-doped carbon.^[43,46,47] The best HER has been reported for the Cs₂AgBiBr₆/2.5%RGO system providing around 490 μmol g⁻¹ h⁻¹ of hydrogen under solar illumination in HBr employing a 300 W illumination and with an apparent quantum efficiency (AQE) of 0.16%.^[46] The present Cs₂AgBiCl₆/10% g-C₃N₄ composite, with an AQE of 2.3% (under 500 W illumination), provides a high hydrogen photogeneration of about 625 μmol g⁻¹ h⁻¹ indicating an effective HCl splitting by a lead-free double perovskite. This is comparable to the data reported so far for HBr or HI splitting but, clearly, is more

appealing from an applicative point of view being the hydrogen evolved in HCl.^[9] Long-term testing up to 16 h confirmed the stability of the hydrogen photogeneration providing a value close to 600 $\mu\text{mol g}^{-1} \text{h}^{-1}$. Stability of the best-performing heterojunction, namely $\text{Cs}_2\text{AgBiCl}_6/10\% \text{ g-C}_3\text{N}_4$, has been checked by collecting XRD data after the photocatalytic experiment showing the preservation of the crystal structure (Figure S1b, Supporting Information).

The reduction of nitrogen to ammonia, as mentioned, follows a different trend along with composition variation (Figure 1c), with a gradual increase of the NH_3 generation rate starting from pure $\text{Cs}_2\text{AgBiCl}_6$ up to the $\text{Cs}_2\text{AgBiCl}_6/90\% \text{ g-C}_3\text{N}_4$ composite, reaching a maximum value of about 40 $\mu\text{mol g}^{-1} \text{h}^{-1}$ at this composition. Pure $\text{g-C}_3\text{N}_4$ nanosheets, or lower amounts of perovskite in the composite (see the point at 5 wt%), perform significantly less effectively. Also in this case, by looking at the nitrogen fixation results of the pure compounds, it is possible to unveil an effective synergy between the two semiconductors. As mentioned, there are no previous reports about nitrogen reduction by a MHP-based heterojunction. However, $\text{g-C}_3\text{N}_4$ has been reported as a suitable material for this reaction, in particular thanks to the presence of nitrogen vacancies.^[48,49] Therefore, $\text{g-C}_3\text{N}_4$ nanosheets used to prepare the present samples have been synthesized to promote the presence of such defects (see Experimental Section), as determined by electron paramagnetic resonance (EPR) experiments (see Figure S5, Supporting Information). The presence of nitrogen vacancies is confirmed by the appearance of an EPR signal related to the number of unpaired electrons directly correlated to the defect formation.^[49] The presence of nitrogen vacancies was further confirmed by X-ray photoelectron spectroscopy (XPS) carried out on a bulk sample of $\text{g-C}_3\text{N}_4$ and on the present nanosheets. The N/C ratio decreased from 1.59 to 1.15 further confirming the formation of nitrogen vacancies.^[50]

From a quantitative point of view, previously reported NH_3 production rates of pure $\text{g-C}_3\text{N}_4$ or of heterojunctions including $\text{g-C}_3\text{N}_4$, are higher than those obtained here. However, it is important to stress a delicate point related to the method employed to measure the photogenerated NH_3 . Currently, most of the reports about ammonia production by nitrogen fixation make use of colorimetric methods which are known to be possibly affected by several interfering compounds, in particular in presence of a sacrificial agent (which should be removed according to ref. 46 before the analysis) and when employing catalysts containing nitrogen such as $\text{g-C}_3\text{N}_4$.^[51,52] In the present article, we devised and optimized an analytical method based on ammonia ion selective electrode (ISEE, for the details see the Experimental Section) to determine the produced ammonia and thus the efficiency of the nitrogen reduction reaction. The ammonia ISE method was preferred to the colorimetric ones (Nessler's reagent and indophenol blue methods) as it is highly sensitive and selective in controlled experimental conditions (temperature, stirring rate, pH, ionic strength, and equilibration time) and not affected by the sacrificial agents and/or by-products.

The results reported earlier demonstrate the suitability of the novel $\text{Cs}_2\text{AgBiCl}_6/\text{g-C}_3\text{N}_4$ system for the photocatalytic hydrogen and ammonia productions indicating, however, a different trend in the production rates as a function of composition.

To understand the mechanisms underpinning the two reactions and the charge carrier dynamics, we afforded a detailed spectroscopic and computational modeling analysis.

The UV-Vis absorption spectra and the Tauc plots for the samples of the $\text{Cs}_2\text{AgBiCl}_6/\text{g-C}_3\text{N}_4$ system are shown in Figure S6, Supporting Information. The band gap of $\text{Cs}_2\text{AgBiCl}_6$ is 2.67 eV while that of $\text{g-C}_3\text{N}_4$ is 2.78 eV, in agreement with previous reports.^[44,45] According to the relative weight ratio in the composite, the gap lies closer to that of the perovskite or the carbon nitride, without significant variations between the values of the two pure compounds.

The normalized photoluminescence spectra of the $\text{Cs}_2\text{AgBiCl}_6/\text{g-C}_3\text{N}_4$ system are reported in Figure 2. The emission is dominated by the broad and intense features of graphitic carbon nitride even at very high perovskite loadings. Such broad spectra, which completely cover the weak perovskite emission, derive from the superimposition of multiple electronic transitions.^[53] In particular, three transitions have been modeled in pristine $\text{g-C}_3\text{N}_4$: a high energy one, centered at around 444 nm, which derives from the relaxation of δ^* electrons to the LP state, and two low energy transitions centered at 455 and 505 nm. To access these low-energy transitions a non-radiative mechanism to populate the π^* state is required, thus the structure of the broadband spectrum depends on the efficiency of this process. In previous works, the interplay between the density of defects and the non-radiative population of π^* state has been studied and related to the photocatalytic properties of $\text{g-C}_3\text{N}_4$.^[53] Composites with lead-free perovskites have also been investigated, with particular focus on the population of non-radiative states and its impact on photocatalytic efficiency.^[19]

Despite the dominant behavior of the graphitic carbon nitride emission, a close inspection of the spectral region around the emission band peak (inset of Figure 2), shows that, for low loadings of perovskite in the composites, there was a reduction of low-lying sub-band population, as the emission displays a stronger contribution from the high energy transition. Conversely, by

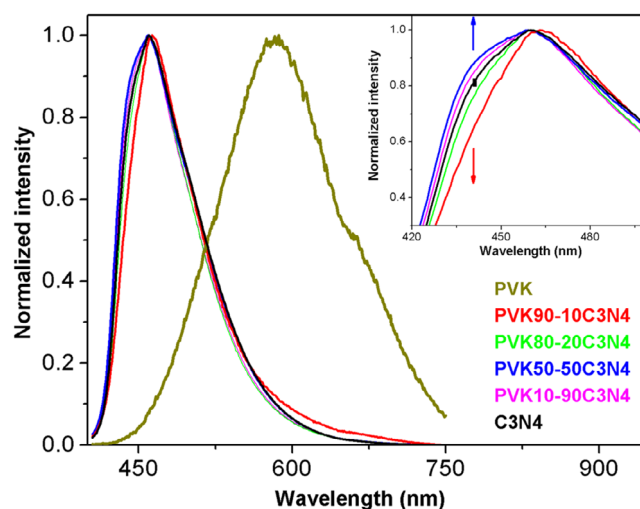


Figure 2. Emission spectra of $\text{Cs}_2\text{AgBiCl}_6/\text{g-C}_3\text{N}_4$ composites powders at different percentages of perovskite loading (wt%). $\text{g-C}_3\text{N}_4$ and $\text{Cs}_2\text{AgBiCl}_6$ refer to pristine materials. $\lambda_{\text{ex}} = 375 \text{ nm}$. Inset: zoom on an interesting spectral zone. PVK stays for $\text{Cs}_2\text{AgBiCl}_6$.

increasing the perovskite content, the low-energy transitions became more and more pronounced. In Figure 2 we reported only some representative samples, but the composite 90–10 Cs₂AgBiCl₆-g-C₃N₄ with the best HER performance was also the sample with the weaker contribution to the broad band by the $\delta \rightarrow ^* \text{LP}$ state transition. These observations point out the effect of perovskite inclusion in funneling optical excitations to the sites where they can be exploited in photocatalytic processes. To further deepen the relations between the excited state dynamics and Cs₂AgBiCl₆/g-C₃N₄ composition, differential transmission (DT) measurements were also performed. Optical excitations were injected with 100-femtosecond laser pulses, 360 nm in wavelength and 1 kHz in repetition rate. A white light supercontinuum was employed as broadband probe (see Experimental Section). DT was directly performed on the solutions, with the same concentration used for photocatalytic studies, i.e. 1 g L⁻¹ in the case of H₂ production (Figure 3a) and 0.5 g L⁻¹ in the case of NH₃ production (Figure 3b).

Full spectrograms obtained from a DT measurement are reported in Figure S7, Supporting Information, while relevant DT spectra extracted at 1 ps delay are reported in Figure 3. The DT spectrum for the pure perovskite sample is characterized by a broadband photoinduced absorption feature, due to absorption from excited states. The 90–10 Cs₂AgBiCl₆-g-C₃N₄ composite, optimized for H₂ generation, has an enhanced photoinduced signal with respect to the pure perovskite sample. This suggests that g-C₃N₄ helps in keeping optical excitations in the perovskite and that the HER occurs at perovskite sites.

In contrast, in samples optimized for nitrogen reduction, shown in Figure 3b, the signal is maximum in the case 10–90 Cs₂AgBiCl₆-g-C₃N₄, i.e., the composition providing the highest NH₃ production rate. Opposite to what is inferred from Figure 3a, in this case, the response is analogous to that of g-C₃N₄, but with an enhanced signal. This suggests that ammonia generation occurs at graphitic carbon nitride sites, but the concentration of optical excitations in carbon nitride, and thus

the ammonia generation rate, is enhanced by the presence of perovskite with respect to pure g-C₃N₄.

As a general observation, the combination between g-C₃N₄ and the perovskite enhances the DT signal of the component actively involved in the reactions. Measurements were repeated for different compositions, and the maximum value of the DT signal was extracted for the two different features of the spectrum, i.e., the one at 500–520 nm and the one at 630–650 nm, as reported in Figure 4. In the case of composites optimized for HER, the spectrum mainly consists of photoinduced absorption (negative DT, thus positive differential absorption DA = -DT) and evolves on a picosecond timescale, as shown in Figure 4a.

Interestingly, the trend of the DA signal as a function of composition was closely related to the trend of HER efficiency. In the case of composites optimized for ammonia generation, a relevant correspondence was found instead between the NH₃ production efficiency and the peak of DT signal at a long time delay (above 1 ns), as shown in Figure 4b. This observation confirms that, for NH₃ production, the photoinjected carriers, which are always generated in the perovskite, are transferred to the g-C₃N₄, where the ammonia evolution reaction occurs, within a nanosecond timescale. Additional relevant data reporting the whole DT decay for different compounds and spectra extracted at longer time delay can be found in Supporting Information (Figure S8 and S9, Supporting Information).

We performed density functional theory (DFT) calculations to rationalize the trends in hydrogen and ammonia production rates with varying g-C₃N₄ concentrations. All calculations have been carried out at a high level of accuracy using hybrid PBE0 functional for geometry optimization with refined HSE06 + SOC calculations for single point energies, as summarized in the Computational Details section. We start with consideration of the pure Cs₂AgBiCl₆ phase. Notably, the standalone Cs₂AgBiCl₆ generates a substantial amount of hydrogen, see Figure 1c. Recent studies have pointed out halide vacancies as potential defects controlling the hydrogen production in the bromide-based analogue Cs₂AgBiBr₆.^[54,55] Theoretical studies

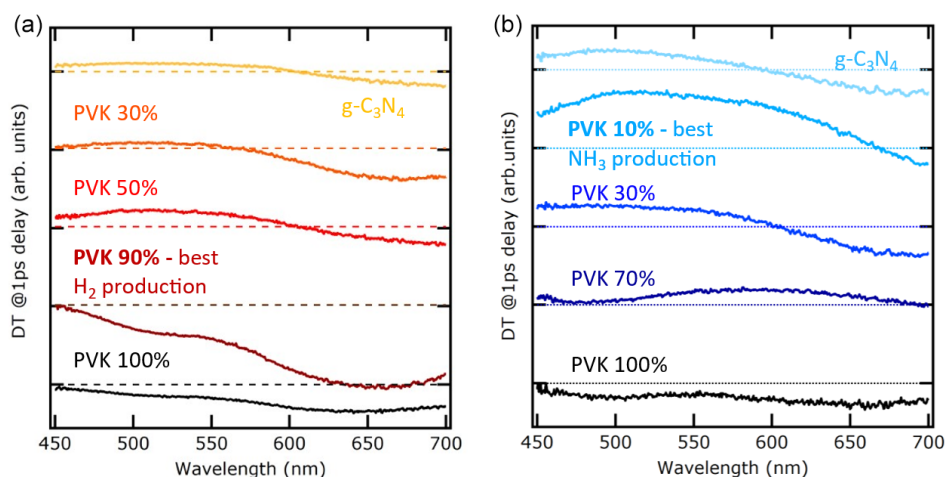


Figure 3. a) Results ranging from 100% Cs₂AgBiCl₆ perovskite (black line) to 100% g-C₃N₄ (yellow line), with the 90–10 PVK-g-C₃N₄ case corresponding to the best HER. b) Results ranging from 100% Cs₂AgBiCl₆ perovskite (black line) to 100% g-C₃N₄ (light-blue line) highlighting the one with 10–90 PVK-g-C₃N₄, corresponding to the best nitrogen reduction. Spectra are reported on the same scale, with zero offset for better readability, with dashed horizontal lines representing the zero for the spectrum of the same color. PVK stands for Cs₂AgBiCl₆.

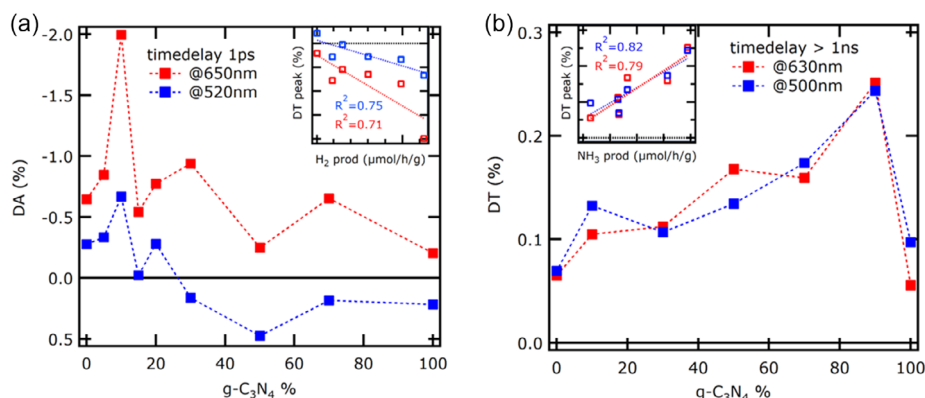


Figure 4. a) Maximum of DA (DT with a minus sign) extracted at 1 ps time delay for different composites as a function of $g\text{-C}_3\text{N}_4$ amount; b) Maximum of DT extracted at time delay >1 ns. The colors of markers are indicating the DA (DT) wavelength ranges 500–520 nm region (blue) and 630–650 nm (red). The insets show the linear correlation between DT peaks amplitude and production rates, with R^2 linear correlation coefficients, with the same color legends as the main plots.

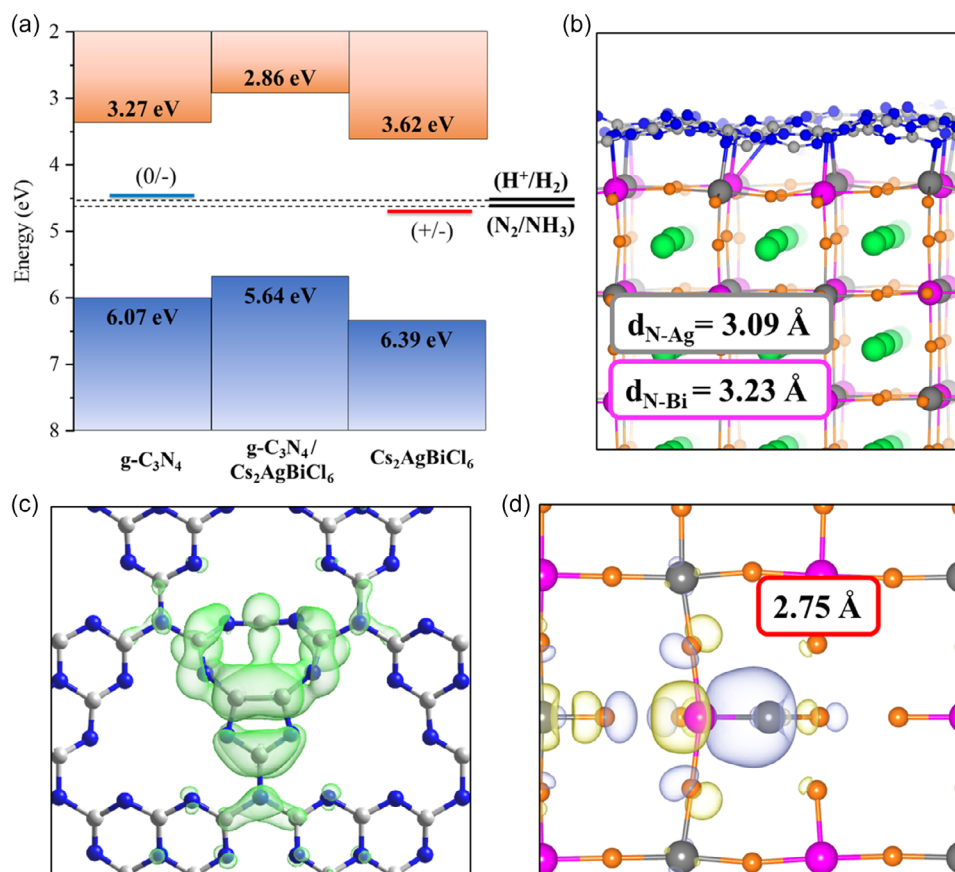


Figure 5. a) Band alignment of $g\text{-C}_3\text{N}_4$, $\text{Cs}_2\text{AgBiCl}_6$, and the $g\text{-C}_3\text{N}_4/\text{Cs}_2\text{AgBiCl}_6$ interface. H^+/H_2 and N_2/NH_3 redox levels as well as thermodynamic transition levels for the nitrogen vacancy, V_N , and the chloride vacancy, V_Cl , are explicitly visualized in the respective phases. Values are referred to the vacuum level; b) Optimized $g\text{-C}_3\text{N}_4/\text{Cs}_2\text{AgBiCl}_6$ interface reporting the average bond lengths for N–Ag and N–Bi; c) Isodensity plot of the unoccupied state of the neutral nitrogen vacancy V_N responsible for electron trapping in the $g\text{-C}_3\text{N}_4$; d) Isodensity plot of the localized state related to the negatively charged V_Cl^- , resulting in the formation of a Ag–Bi dimer with 2.75 Å bond length.

further showed low-formation energies of chloride vacancies, V_Cl , in $\text{Cs}_2\text{AgBiCl}_6$ bulk phases.^[56] We modeled chloride vacancies in different charge states at a (001)-surface of $\text{Cs}_2\text{AgBiCl}_6$

with $(\text{Ag}_{0.5}\text{Bi}_{0.5})\text{Cl}_2$ -termination, see Figure S10 and Table S2, Supporting Information. Our calculations predict deep (+/-) transition levels for a surface V_Cl at 1.7 eV above the valence band

maximum, see Figure 5a. V_{Cl} in its negative charge state forms a stable Bi–Ag dimer by trapping 2 electrons, see Figure 5d and S11, Supporting Information. These electrons are localized at surface defects and likely are key for hydrogen evolution, as previously reported for Sn–Sn dimers in tin-halide perovskites.^[15] The respective (+/–) transition further matches fairly with the experimental photoinduced signals, Figures 3a and 4a. Furthermore, our DFT calculations predict the formation of self-trapped excitons, see Figure S12 and Table S3, Supporting Information, being - together with emission from halide vacancies-responsible for the broad emission features in the pure $Cs_2AgBiCl_6$ phase, Figure 2, in line with previous reports.^[57–59]

To rationalize the trend in HER, we study the band alignment of the $g-C_3N_4/Cs_2AgBiCl_6$ heterostructure for the $Cs_2AgBiCl_6$ with and without the $g-C_3N_4$ monolayer adsorbed, representative for the low and high-wt% of $g-C_3N_4$ regions, respectively; see Figure 5a and S13, Supporting Information, for model setup. The band edges of $Cs_2AgBiCl_6$ at the $g-C_3N_4/Cs_2AgBiCl_6$ interface appear favorable for charge separation, as the conduction band minimum (CBM) of $g-C_3N_4$ lies energetically lower (3.27 eV) than the one of $g-C_3N_4/Cs_2AgBiCl_6$ (2.86 eV), in line with the density of states of the heterostructure model, Figure S13c, Supporting Information. This results in electron transfer from the perovskite absorber to $g-C_3N_4$. Moreover, a large offset in band edges of the $g-C_3N_4/Cs_2AgBiCl_6$ to the $Cs_2AgBiCl_6$ itself is present, suggesting a driving force for electrons from the interface to the $Cs_2AgBiCl_6$ bulk. Increasing the amount of $g-C_3N_4$ may consequently increase the lifetime of charge carriers due to efficient charge separation, but also suppresses the formation of self-trapped excitons (STEs) as seen experimentally, Figure 2, resulting in the increase in HER, Figure 1c.

Our DFT calculations of the $g-C_3N_4/Cs_2AgBiCl_6$ heterostructure show a strong binding of the $g-C_3N_4$ on the $(Ag_{0.5}Bi_{0.5})Cl_2$ -terminated $Cs_2AgBiCl_6$ surface with a formation energy of -4.22 eV nm^{-2} , mediated by formation nitrogen-metal bonds with average bond length of 3.09 and 3.23 Å for N–Ag and N–Bi, respectively, see Figure 5b. Consequently, reactive V_{Cl} surface sites are passivated upon increase of $g-C_3N_4$ and further proton transport to the $Cs_2AgBiCl_6$ surface may be effectively hindered, reducing the evolution of H_2 . Note that already a small wt% of $g-C_3N_4$ may be sufficient to cover the $Cs_2AgBiCl_6$ surface to a large extent, as we estimated from a toy model based on geometrical considerations, see Figure S14, Supporting Information. Controlling the wt% of $g-C_3N_4$ consequently results in an ideal composition that balances efficient charge separation and carrier lifetime as well as the access to active catalytic sites, thereby maximizing the HER.

Considering the rate of NH_3 production, we observe a different trend compared to H_2 production, Figure 1c. Initially, the presence of $g-C_3N_4$ alone is sufficient to generate few amounts of NH_3 . Considering the band alignment, electrons should jump from the $Cs_2AgBiCl_6$ to the $g-C_3N_4$. As potential active sites, we calculated the formation of nitrogen vacancy in $g-C_3N_4$, resulting in V_N^0 formation energies of 3.36 eV, see Table S5, Supporting Information, which is in good agreement with previous studies.^[60–62] The nitrogen vacancy introduces localized energy

levels within the band gap, see Figure S15, Supporting Information, and introduces a $(0/-)$ transition at 1.56 eV, see Table S5, Supporting Information. Importantly, the $(0/-)$ level of nitrogen vacancies are close to the redox potential for N_2/NH_3 (reported by dashed line in Figure 5a), suggesting a plausible mechanism for the initial steps in the photofixation mechanism. Upon addition of $Cs_2AgBiCl_6$, the catalytic activity is enhanced which we may attribute to the superior absorbance of the $Cs_2AgBiCl_6$ perovskite. At highest perovskite concentration, surface defects of the $Cs_2AgBiCl_6$ likely compete with the electron transfer to $g-C_3N_4$, limiting NH_3 production. This observation highlights the delicate balance required for optimal performance in the heterostructure system, requiring a fine tuning of the heterostructure composition.

3. Conclusions

$Cs_2AgBiCl_6/g-C_3N_4$ heterojunctions for hydrogen photogeneration and nitrogen reduction to ammonia have been investigated through advanced spectroscopy and computational modeling, aiming at unveiling the mechanism of these reactions. DT measurements provided detailed information on the charge carrier dynamics in the heterojunction indicating that for high perovskite amounts, best-performing compositions for H_2 photogeneration, the optical excitations are confined on the $Cs_2AgBiCl_6$, where the reaction occurs. The opposite situation is found for systems containing a low amount of $Cs_2AgBiCl_6$ (high $g-C_3N_4$), which best perform for nitrogen reduction, where the typical DT signal of $g-C_3N_4$ results to be enchanted. This finding suggests that active sites for ammonia production are confined in the carbon nitride. The trend of DA signal as a function of the composition well follows the trend of photoproduction of the two reactions. DFT calculations show that the active sites for HER are chloride vacancies, V_{Cl} , and that the coupling to $g-C_3N_4$, thanks to a favorable band alignment at the interface, increases the lifetime of charge carriers and suppresses STE of $Cs_2AgBiCl_6$. The positive effect of the heterojunction formation in promoting hydrogen photogeneration is however progressively lost by increasing the amount of $g-C_3N_4$ due to a passivating effect of the V_{Cl} . Such mechanistic insight correlates well with the trend of HER of the $Cs_2AgBiCl_6/g-C_3N_4$ heterojunction and confirms the active role of the perovskite in this reaction. In contrast, DFT calculations confirm the role of nitrogen vacancies as the active sites for nitrogen reduction. In this case, the positive effect of small perovskite amounts is mostly related to its superior light absorbance and further increase of $Cs_2AgBiCl_6$ amounts progressively reduces the ammonia generation rate promoting the charge funneling toward perovskite active sites, in good agreement with experimental results.

Overall, this study on photoactive heterojunctions including a perovskite and graphitic carbon nitride provides a detailed microscopic insight into the reaction mechanisms, pointing out the key role of the system composition tuning in tailoring different photocatalytic reactions including, for the first time, the photoreduction of nitrogen to ammonia by a perovskite-based heterojunction.

4. Experimental Section

4.1. Sample Synthesis, Structural and Morphological Characterization

Nanosheets g-C₃N₄ has been synthesized from the bulk form (bulk g-C₃N₄) with a polymerization of Dicyandiamine DCD (NH₂C(=NH)NHCN, Aldrich, 99%) by the following thermal treatment under N₂ flux: heating (1 °C min⁻¹) to a selected temperature of 550 °C, the isothermal step for 4 h followed by cooling to room temperature (10 °C min⁻¹). The synthesis was carried out in a partially closed alumina crucible. The thermal exfoliated catalyst (nanosheets) was prepared by heating to a selected temperature of 500 °C with an isothermal step for 2 h the bulk g-C₃N₄ in air. The Cs₂AgBiCl₆/nanosheets g-C₃N₄ composite has been synthesized dissolving a stoichiometric ratio of the precursor salts AgCl (Aldrich 99%), BiCl₃ (Aldrich 99%) and CsCl (Aldrich 99%) in organic solvent *N,N*-dimethylformamide (DMF) and dried under vigorous stilling at 65 °C. This polar solvent can dissolve most organic and inorganic salts and may be suitable for the cations that are insoluble in HCl. The composites series have been realized changing the percentage of the perovskite (Cs₂AgBiCl₆) and the nanosheets g-C₃N₄ (g-C₃N₄ ns) in the composites: 100% Cs₂AgBiCl₆, 90% Cs₂AgBiCl₆ –10% g-C₃N₄, 80% Cs₂AgBiCl₆ –20% g-C₃N₄ ns, 50% Cs₂AgBiCl₆ –50% g-C₃N₄ ns, 30% Cs₂AgBiCl₆ –70% g-C₃N₄ ns, 10% Cs₂AgBiCl₆ –90% g-C₃N₄ ns. The crystal structure of the samples has been characterized by room temperature Cu-radiation XRD acquired with Bruker D2 diffractometer. Small shifts in the patterns of Figure 1a are related to zero-shift error which has been taken into account during pattern analysis. DRS spectra were acquired in the wavelength range 300–800 nm directly on the powders by using a Jasco V-750 spectrophotometer, equipped with an integrating sphere (Jasco ISV-922). Microstructural characterization of the samples was made using a high-resolution scanning electron microscope (SEM, TESCAN Mira 3) operated at 25 kV.

4.2. Hydrogen Evolution Experiments

H₂ evolution experiments were conducted in 37% HCl-50% H₃PO₂ (5:1, v/v) solutions (concentrated acids were from Aldrich) irradiated in Pyrex glass containers (36 mL capacity, 24 mL sample). After addition of the catalyst (1 g L⁻¹), the sample was deoxygenated by Ar bubbling (20 min) to obtain anoxic conditions and irradiated under magnetic stirring for 4 h. Chloroplatinic acid (H₂PtCl₆, 38% Pt basis) was added as precursor for metallic Pt (Aldrich). Since Pt is in situ photodeposited on the catalyst surface, after Ar bubbling a small volume from a 14 g L⁻¹ H₂PtCl₆ aqueous solution was added by a 10–100 μL micropipette to the catalyst suspension, corresponding to 3% w/w Pt. Each photoreactor was closed with sleeve stopper septa and irradiated, as described in the following, achieving simultaneous Pt deposition and H₂ production.^[63]

Irradiation was performed under simulated solar light (1500 W Xenon lamp, 300–800 nm) using a Solar Box 1500e (CO.FO.ME.GRA S.r.l., Milan, Italy) set at a power factor 500 W m⁻², and equipped with UV outdoor filter made of IR-treated soda lime glass. Triplicate photoproduction experiments were

done on all samples. The headspace evolved gas was quantified by gas chromatography coupled with thermal conductivity detection (GC-TCD), as detailed in previous work.^[64] The results obtained in terms of H₂ evolution rate (HER) are expressed in the paper as μmol of gas per gram of catalyst per hour (μmole g⁻¹ h⁻¹). The kinetics of H₂ formation, studied for the best performing composite through duplicate experiments, is reported in Figure S16, Supporting Information. The photon flux, measured as previously reported,^[65] was 1.53 × 10⁻⁷ photons moles s⁻¹. The apparent quantum yield (AQY), calculated as the percent ratio H₂ moles/incident photons moles,^[59] was 2.3% for the composite giving the highest H₂ evolution.

4.3. Nitrogen Photofixation Experiments

N₂ photofixation experiments were conducted in tridistilled water containing 10% v/v methanol (Aldrich, ≥99.9%) irradiated in Pyrex glass container (250 mL capacity, 100 mL sample). After addition of the catalyst (0.5 g L⁻¹), the sample suspension was deoxygenated by N₂ bubbling (45 min) to obtain a saturated solution and then irradiated under magnetic stirring for 3 h maintaining the temperature at 15 °C. For the experiments involving use of 1% w/w Pt co-catalyst, the same Chloroplatinic acid (H₂PtCl₆, 38% Pt basis) was added as precursor for metallic Pt (Aldrich). The quantification was performed with ammonia ion selective electrode, as reported below.

4.4. Ammonia Determination

The Thermo Scientific Orion Ammonia Ion Selective Electrode (ISE) was selected as it measures ammonia ions in aqueous solutions quickly, simply, economically, and accurately.

The ammonia ISE uses a hydrophobic gas-permeable membrane which separates the sample solution from the electrode filling solution. Water does not wet the membrane and does not penetrate the holes, whereas the dissolved ammonia in the sample solution diffuses through the membrane until the partial pressure of ammonia is the same on both sides of the membrane. In any sample the partial pressure of ammonia is proportional to its concentration.

Daily freshly tridistilled water,^[46] free of volatile amines that can positively interfere with the measurements, was used for all standards and samples. The pH of all standards and samples was adjusted above 11 with a strong base (10 N NaOH) to quantify ammonia in its uncharged form, viz. NH₃(aq). Standard solutions and samples had ionic strength <1 M with about the same level of ions and dissolved species. The ionic species cannot cross the membrane but can change the solubility of ammonia and/or form metal complexes. Most of metals are removed in the form of hydroxide complexes or precipitates in the basic solution.

All measurements were performed in a beaker with minimized surface area/volume ratio, at a uniform and moderate rate, under controlled temperature. Since a change in temperature can cause a change of the slope and potential, a piece of insulating material, e.g., ceramic or cardboard, was placed between the magnetic stirring plate and beaker to prevent measurement errors from transfer of heat to sample.

In details, ISE was immersed in the solution (standard or sample, 1% v/v 10 N NaOH, 10% v/v MeOH) until a stable potential value (mV) was obtained (at least 2 or 3 min). For the quantification, a calibration curve was daily constructed plotting the mV value recorded against the Log Concentration, to verify the slope (varying in the range $-54 \div -60$ mV). The ammonia concentration in the sample was further assessed by two standard additions. Figure S17, Supporting Information, reports an example of mean calibration curve ($0.25 \text{ mg L}^{-1} \div 10 \text{ mg L}^{-1}$ as NH_3). The influence of different parameters was carefully investigated to exclude any possible interferences on the quantification of ammonia in solution. Sample colour and turbidity did not affect the ISE quantification, as experimentally verified by measurements on both filtered and not-filtered samples obtaining not significantly different NH_3 concentrations ($p < 0.05$). Therefore, the final method was applied to not filtered samples. On the contrast, coloured or cloudy solutions lead to an overestimation of the NH_3 concentration in spectrophotometric assays. The effect of methanol, used as sacrificial agent, and its by-products, namely formaldehyde and formic acid, was evaluated by constructing calibration curves. Accordingly, standard solutions were prepared in presence of MeOH in the range $1 \div 20\%$ v/v, HCHO in the range $0.01 \text{ mg L}^{-1} \div 10 \text{ mg L}^{-1}$ and formic acid $0.001 \div 0.1\%$ v/v, respectively. The slope of each curve was compared with the one obtained in ultrapure water, achieving not significantly different values ($p < 0.05$). On the contrary, when using the colorimetric Nessler's reagent method, methanol interferes heavily, resulting in an overestimation of the NH_3 concentration,^[46] and herein experimentally verified.

4.5. Ag and Bi Leaching Tests

The leaching tests were performed by dispersion of the perovskite powder in distilled water, under magnetic stirring for 4 h. Then the suspension was filtered on $0.2 \mu\text{m}$ nylon membrane and the amount of Ag and Bi in solution was determined by ICP-OES, after acidification (1% v/v ultrapure nitric acid). The $\text{Cs}_2\text{AgBiCl}_6$ perovskite resulted stable, with a leaching $<0.1\%$ for Ag and $<0.05\%$ for Bi. As silver could interfere by complexing ammonia, leaching tests were also performed on all the $\text{g-C}_3\text{N}_4/\text{Cs}_2\text{AgBiCl}_6$ composites, highlighting a negligible Ag release ($<0.9\%$) also for the best performing material with negligible complex formation, further confirmed by ISE measurements, in NaOH/EDTA in place of NaOH solution.

4.6. Ultrafast Spectroscopy Measurements

DT measurements were performed on the composite solution in a pump and probe configuration. Ti:Sapphire laser (Libra – Coherent) delivering 100 fs pulses at 800 nm with 1 kHz repetition rate is sent to a tunable parametric optic amplifier (TOPAS - Light Conversion) to get pulses at the chosen excitation wavelength (360 nm). The measurement is performed with two different configurations to explore two different delay range: 1) Helios (Ultrafast Systems) with optical delay line (max 8 ns delay), where supercontinuum white probe pulses are derived by focusing the 800 nm laser on a Sapphire crystal, thus allowing for sub-ps resolution. 2) EOS (ultrafast Systems) with digitally controlled

delay (max 1 ms delay), with white probe pulses generated by means of a fibre laser.

DT transmitted and reference spectra are collected with two spectrometers coupled to CMOS detectors, in differential configuration. The samples are analysed in form of solution, which is first sonicated for 15 min and then poured into a 1 mm thick quartz cuvette. The concentration of the composites is the same used for the photocatalytic measurements, i.e. 1 g L^{-1} in the case of HER and 0.5 g L^{-1} in the case of NH_3 photofixation.

5. Computational Details

5.1. DFT Calculations

DFT calculations have been carried out for the $\text{Cs}_2\text{AgBiCl}_6$ and $\text{g-C}_3\text{N}_4$ phases, the interface, and defects in the supercell approach. Ionic positions were optimized using the CP2K software package using the PBE0 exchange-correlation functional and by including DFT-D3 dispersion corrections.^[66–69] For $\text{g-C}_3\text{N}_4$, we employ an orthorhombic $2 \times 2 \times 2$ supercell with $a = 7.08 \text{ \AA}$, $b = 12.27 \text{ \AA}$, $c = 6.97 \text{ \AA}$; for $\text{Cs}_2\text{AgBiCl}_6$, we use the cubic phase with $a = b = c = 10.77 \text{ \AA}$.^[18,44] In all cases, geometry optimization was carried out at the Γ -point of the Brillouin zone. We used the Goedecker–Teter–Hutter (GTH) norm-conserving pseudopotentials and MOLOPT double-zeta Gaussian basis sets.^[70,71] The auxiliary density matrix method has been used to accelerate calculations with the hybrid PBE0 functional.^[72]

To refine the defect formation energies and thermodynamic ionization levels, single-point DFT calculations were carried out using the hybrid HSE06 functional with inclusion of spin-orbit coupling (SOC) corrections on the optimized geometries within the Quantum Espresso software package.^[73] Screening of the fraction of exact exchange of the $\text{Cs}_2\text{AgBiCl}_6$ shows best agreement at a value of $\alpha = 0.31$ with the experimental values, as shown in Table S1, Supporting Information. All calculations were carried out at the Γ point of the Brillouin zone, using norm-conserving full relativistic pseudopotentials with electrons from Cl 5s, 5p; Cs 5s, 5p, 6s; Ag 5s, 5p, 4d; and Bi 6s, 6p, 5d shells explicitly included. Plane-wave basis set cutoffs for the smooth part of the wave functions and the Fock grid of 40 and 80 Ry, respectively, were chosen. Dispersion corrections were accounted for using the D3 scheme.

Defect formation energies (DFEs) and thermodynamic ionization levels (TILs) were calculated within the supercell approach following the expressions:

$$\text{DFE}[X^q] = E[X^q] - E[\text{pristine}] - \sum_i n_i \mu_i + q(\epsilon_{\text{VB}} + \epsilon_{\text{F}}) \quad (1)$$

$$\epsilon(q/q') = \frac{\text{DFE}(X^q|E_{\text{F}} = 0) - \text{DFE}(X^{q'}|E_{\text{F}} = 0)}{q' - q} \quad (2)$$

where $E[X^q]$ is the energy of the supercell with defect X in the charge state q, $E(\text{pristine})$ is the energy of the pristine (non-defective) supercell. n_i and μ_i are the number and the chemical potentials of the species added or subtracted, respectively and ϵ_{VB} is the valence band energy of the pristine system.^[74] The last two terms of Equation (1) represent the energy to the exchange electrons with the Fermi level of the system (ϵ_{F}).

5.2. Model Setup

Firstly, we optimized the pristine structure of g-C₃N₄ using a 3 × 2 supercell, see Figure S10a, Supporting Information. The monolayer was cut along the (001) direction, and an additional 15 Å of vacuum was added perpendicular to the monolayer to prevent interactions with periodic replicas. Similarly, we optimized a slab model of the double perovskite Cs₂AgBiCl₆ using a 2 × 2 in-plane supercell, with (001) direction, and added 15 Å of vacuum to maintain separation from periodic images. Two different surface terminations were investigated for Cs₂AgBiCl₆: (Ag_{0.5}Bi_{0.5})Cl₂ and CsCl, see Figure S10b, Supporting Information.

5.3. Chloride Vacancies in CABC

Considering the Cs₂AgBiCl₆, we specifically investigate a chloride vacancy on the (Ag_{0.5}Bi_{0.5})Cl₂-terminated surface. The vacancy was stable in the positive charge state (+1), and its presence did not significantly alter the lattice structure of Cs₂AgBiCl₆. Upon addition of electrons, we observe the formation of an Ag–Bi dimer. In the neutral state, the dimer shows a distance of 2.82 Å, while in the negatively charged state, the distance is reduced to 2.75 Å, shown in Figure S11, Supporting Information. The thermodynamic ionization levels (TILs) for the (+/0) and (+/−) transitions are 1.76 and 1.69 eV above the valence band maximum, respectively, indicating a deep trap state associated with the defect, see Table S2, Supporting Information. As highlighted in the main text of our research, this specific defect holds significant implications as an active site for H₂ production.

We further investigate the geometry of the V_{Cl}[−] on the Cs₂AgBiCl₆ surface upon inclusion of SOC corrections, as SOC could potentially destabilize the formation of metal dimers as known for the lead-halide perovskites.^[75] We optimize the structure containing the V_{Cl}[−] vacancy using PBE + SOC within the Quantum Espresso software package. Comparison of the PBE0 and PBE + SOC optimized structures suggest the stability of the Ag–Bi dimer, with bond lengths only slightly varying, see Figure S11, Supporting Information. Thus, we can confidently trust the PBE0 structural properties despite neglecting SOC.

5.4. Self-Trapped Excitons

We investigate the formation of STEs upon illumination. Figure S13a, Supporting Information, summarizes the STE formation mechanism. Optimizing the system in the triplet state, using the PBE0 functional, results in the localization of the exciton, see Figure S13b, Supporting Information. The localization of the electron Kohn–Sham orbital is accompanied by an increase in Bi–Cl bond lengths from 2.7 Å to above 3.0 Å, see Figure S13b, Supporting Information. Similarly, the hole Kohn–Sham orbital localized within strongly shortened axial Ag–Cl bonds of 2.3 Å, see Figure S13b, Supporting Information. The calculated emission signal is of 1.46 eV while the estimated absorption is at 2.8 eV, see Table S3, Supporting Information. Note that halide vacancies likely strongly contribute to the emission. Self-trapping of excitons is key to observing broad emission features, while the

detailed contribution of STEs or by recombination from halide vacancies is still under debate.^[76,77]

5.5. Interface Model

Finally, we model the interface between the g-C₃N₄ and Cs₂AgBiCl₆ to gain insight into the structural and electronic modifications upon interface formation. The lattice constants of g-C₃N₄ and Cs₂AgBiCl₆ nicely match along the *a* direction, while the *b* direction shows substantial differences in the lattice constants of 13%. Thus, we cut the g-C₃N₄ layer along the *b*-direction and passivate undercoordinated N atoms with H atoms, see Figure S13b, Supporting Information. This ensures maximal coverage without introducing artificial strain into the g-C₃N₄. Considering the electronic properties, we obtain a band gap of 3.22 eV for the modified g-C₃N₄, which is in excellent agreement with the fully periodic g-C₃N₄ monolayer (3.4 eV). We passivated both surfaces in the perovskite slab with the modified g-C₃N₄ layers. We initially performed single-point calculations at different distances between the Cs₂AgBiCl₆ and the g-C₃N₄, as well as for different horizontal alignments for g-C₃N₄. Starting from the low energy configuration, geometry optimization was performed, resulting in a strongly bound heterostructure with a binding energy of −4.22 eV nm^{−2}. Looking closer at the structure shows that each undercoordinated surface metal ion is successfully passivated (see Figure 5b and S13a, Supporting Information of the manuscript). The DOS shown in Figure S13c, Supporting Information, shows a type II band alignment with the VB and CB of g-C₃N₄ below the ones of the perovskite layer.

The large binding energy presents an interesting hypothesis that may explain the observed drop in the H₂ production rate when adding a small weight percentage of g-C₃N₄. To estimate the surface coverage, we derive a simple toy system relying on pure geometric considerations, shown in Figure S14b, Supporting Information. We assume cubic nanocrystals of Cs₂AgBiCl₆. The nanocrystal surface area is given by 6L², where L represents the nanocubes dimension. The g-C₃N₄ is modeled as 2D rectangular layers, which may passivate the surfaces of the perovskite nanocubes. The given wt% of g-C₃N₄ allows us to calculate the surface ratio of the Cs₂AgBiCl₆ to the g-C₃N₄, as shown in Figure S14a, Supporting Information. Our model system indicates that substantial coverage of the nanocrystal surface can already be achieved at low wt%. This suggests that the passivation of the surface may inhibit the catalytic active site of Cs₂AgBiCl₆ due to a small amount of g-C₃N₄.

5.6. Nitrogen Vacancies in g-C₃N₄

In g-C₃N₄, three nitrogen atoms can be removed to create vacancies: N1, nitrogen being bonded to three carbon atoms connecting three heptazine flakes; N2, nitrogen being bonded to only two C atoms; and N3, nitrogen being removed from inside a heptazine sub-structure. To determine the most stable state, we considered the neutral state of the vacancy and examined the various possible spin states. Our analysis reveals that the N3 vacancy in a doublet spin state is the most stable, as shown in Table S4, Supporting Information.

We further determine the thermodynamic ionization level of N₂ and N₃ vacancies by calculating the negative charge state by adding an electron. DFEs provide insights into the thermodynamic stability and formation abilities of specific defects. In contrast, TILs represent the redox potential associated with the capture of carriers at defect sites. For both defects considered, the (0/-) transition is found to be deep within the band gap, see Table S5, Supporting Information. This implies that the nitrogen vacancies can trap electrons, localized state within the band gap of the monolayer, as shown in Figure S15, Supporting Information. For the monolayer, a band gap value of 3.4 eV was calculated, significantly larger than the experimental values of 2.7 eV due to the dimensionality reduction. To estimate the accuracy of given defects, we calculate the DFEs and TILs of all nitrogen vacancies in a g-C₃N₄ bulk supercell at the same level of theory. The obtained bulk band gap value of 2.9 eV closely aligns with the experimental values, shown in Table S5, Supporting Information. Defect TILs remain deep in the band gap while being shifted downwards in energy.

Supporting Information

Supporting Information is available from the Wiley Online Library or from the author.

Acknowledgements

C.T. and L.G. should be considered joint first author: C.T. has carried out experimental part while L.G. has performed computational simulations. L.M., A.S., and A.P. acknowledge support from the Ministero dell'Università e della Ricerca (MUR) and the University of Pavia through the program "Dipartimenti di Eccellenza 2023–2027". L.M. and A.L. acknowledge financial support under the National Recovery and Resilience Plan (NRRP), Mission 4, Component 2, Investment 1.1, Call for tender No. 1409 published on 14.9.2022 by the Italian Ministry of University and Research (MUR), funded by the European Union - Next Generation EU - Project Title P2022HSWX - A bio-inspired chemical approach for agro-industrial waste valorization (BEAGLE) - CUP F53D23008890001 - Grant Assignment Decree No. 1384 adopted on 1.9.2023 by the Italian Ministry of University and Research (MUR). E.M. acknowledges financial support under the National Recovery and Resilience Plan (NRRP), Mission 4, Component 2, Investment 1.1, Call for tender No. 104 published on 2.2.2022 by the Italian Ministry of University and Research (MUR), funded by the European Union - NextGenerationEU - Project Title 2022HRZH7P - Re-evolutionary solar fuel production envisioning water stable lead-free perovskite exploitation - REVOLUTION - CUP B53D23015350006 - Grant Assignment Decree No. 1064 adopted on 18.7.2022 by the Italian Ministry of University and Research (MUR). A.S. acknowledges financial support under the National Recovery and Resilience Plan (NRRP), Mission 4, Component 2, Investment 1.1, Call for tender No. 104 published on 2.2.2022 by the Italian Ministry of University and Research (MUR), funded by the European Union - NextGenerationEU - Project Title "Towards efficient and cost-effective nitrogen fixation via photocatalysis: insights form experiment and theory - PHOTOFIX - CUP F53D23005160006 - Grant Assignment Decree No. 1064 on 18.7.2022 by the Italian Ministry of University and Research (MUR). S.C. acknowledges financial support under the National Recovery and Resilience Plan (NRRP), Mission 4, Component 2, Investment 1.1, Call for tender No. 104 published on 2.2.2022 by the Italian Ministry of University and Research (MUR), funded by the European Union - NextGenerationEU - Project Title 2022HWW3S-Atomic scale engineering of metal halide perovskites surface towards exceptionally stable and highly selective photo Electrodes for CO₂

conversion into fuels (INTERFACE) - CUP B53D23006040006 - Grant Assignment Decree No. 961 adopted on 30.6.2023 by the Italian Ministry of University and Research (MUR). E.M. and S.C. acknowledge project Ricerca@CNR PHOTOCAT (CUP B93C21000060006). E.M. acknowledges funds for the European Union - NextGenerationEU under the POR H2 AdP project, L.A.1.1.35 (CUP B93C22000630006). F.D.A. acknowledges funds be the European Union - NextGenerationEU under the Italian Ministry of University and Research (MUR) National Innovation Ecosystem grant ECS00000041 - VITALITY. L.M and C.T. acknowledge financial support from R.S.E. SpA (Ricerca sul Sistema Energetico). E.M and A.A.A wish to thank the Distinguished Scientist Fellowship Program (DSFP) of King Saud University, Riyadh, Kingdom of Saudi Arabia.

Conflict of Interest

The authors declare no conflict of interest.

Data Availability Statement

The data that support the findings of this study are available from the corresponding author upon reasonable request.

Keywords

DFT calculations, hydrogen production, nitrogen fixation, perovskite, photocatalysis

Received: February 7, 2024

Revised: March 30, 2024

Published online:

- [1] H. Huang, B. Pradhan, J. Hofkens, M. B. J. Roeffaers, J. A. Steele, *ACS Energy Lett.* **2020**, *5*, 1107.
- [2] K. A. Huynh, D. L. T. Nguyen, V.-H. Nguyen, D.-V. N. Vo, Q. T. Trinh, T. P. Nguyen, S. Y. Kim, Q. V. Le, *J. Chem. Technol. Biotechnol.* **2020**, *95*, 2579.
- [3] B.-M. Bresolin, Y. Park, D. W. Bahnemann, *Catalysts* **2020**, *10*, 709.
- [4] M. Corti, S. Bonomi, R. Chiara, L. Romani, P. Quadrelli, L. Malavasi, *Inorganics* **2021**, *9*, 56.
- [5] J. Yuan, H. Liu, S. Wang, X. Li, *Nanoscale* **2021**, *13*, 10281.
- [6] F. Temerov, Y. Baghdadi, E. Rattner, S. Eslava, *ACS Appl. Energy Mater.* **2022**, *5*, 14605.
- [7] M. Xiao, Y. Zhang, J. You, Z. Wang, J.-H. Yun, M. Konarova, G. Liu, L. Wang, *J. Phys. Energy* **2022**, *4*, 042005.
- [8] Z.-Y. Chen, N.-Y. Huang, Q. Xu, *Coord. Chem. Rev.* **2023**, *481*, 215031.
- [9] L. Romani, L. Malavasi, *ACS Omega* **2020**, *5*, 25511.
- [10] V. Armenise, S. Colella, F. Fracassi, A. Listorti, *Nanomaterials* **2021**, *11*, 433.
- [11] J. Wang, Y. Shi, Y. Wang, Z. Li, *ACS Energy Lett.* **2022**, *7*, 2043.
- [12] M. A. Raza, F. Li, M. Que, L. Zhu, X. Chen, *Mater. Adv.* **2021**, *2*, 7187.
- [13] X. Wang, J. He, X. Chen, B. Ma, M. Zhu, *Coord. Chem. Rev.* **2023**, *482*, 215076.
- [14] C. Tedesco, L. Malavasi, *Molecules* **2023**, *28*, 339.
- [15] D. Ricciarelli, W. Kaiser, E. Mosconi, J. Wiktor, M. W. Ashraf, L. Malavasi, F. Ambrosio, F. De Angelis, *ACS Energy Lett.* **2022**, *7*, 1308.
- [16] H. Fu, X. Liu, Y. Wu, Q. Zhang, Z. Wang, Z. Zheng, H. Cheng, Y. Liu, Y. Dai, B. Huang, P. Wang, *Appl. Surf. Sci.* **2023**, *622*, 156964.
- [17] L. Romani, A. Bala, V. Kumar, A. Speltini, A. Milella, F. Fracassi, A. Listorti, A. Profumo, L. Malavasi, *J. Mater. Chem. C* **2020**, *8*, 9189.

- [18] L. Romani, A. Speltini, F. Ambrosio, E. Mosconi, A. Profumo, M. Marelli, S. Margadonna, A. Milella, F. Fracassi, A. Listorti, F. De Angelis, L. Malavasi, *Angew. Chem., Int. Ed.* **2021**, *60*, 3611.
- [19] L. Romani, A. Speltini, C. N. Dibenedetto, A. Listorti, F. Ambrosio, E. Mosconi, A. Simbula, M. Saba, A. Profumo, P. Quadrelli, F. De Angelis, L. Malavasi, *Adv. Funct. Mater.* **2021**, *31*, 2104428.
- [20] B.-M. Bresolin, C. Günemann, D. W. Bahnemann, M. Sillanpää, *Nanomaterials* **2020**, *10*, 763.
- [21] S. Park, W. J. Chang, C. W. Lee, S. Park, H.-Y. Ahn, K. T. Nam, *Nat. Energy* **2017**, *2*, 16185.
- [22] A. Pisanu, A. Speltini, P. Quadrelli, G. Drera, L. Sangaletti, L. Malavasi, *J. Mater. Chem. C* **2019**, *7*, 7020.
- [23] K. Li, S. Li, W. Zhang, Z. Shi, D. Wu, X. Chen, P. Lin, Y. Tian, X. Li, *J. Colloid Interface Sci.* **2021**, *596*, 376.
- [24] L. Zhou, Y.-F. Xu, B.-X. Chen, D.-B. Kuang, C.-Y. Su, *Small* **2018**, *14*, 1703762.
- [25] Y. Jiang, R. Zhou, Z. Zhang, Z. Dong, J. Xu, *J. Mater. Chem. C* **2023**, *11*, 2540.
- [26] S. Cheng, X. Chen, M. Wang, G. Li, X. Qi, Y. Tian, M. Jia, Y. Han, D. Wu, X. Li, Z. Shi, *Appl. Surf. Sci.* **2023**, *621*, 156877.
- [27] H. Fu, X. Liu, J. Fu, Y. Wu, Q. Zhang, Z. Wang, Y. Liu, Z. Zheng, H. Cheng, Y. Dai, B. Huang, P. Wang, *ACS Catal.* **2023**, *13*, 14716.
- [28] H. Huang, D. Verhaeghe, B. Weng, B. Ghosh, H. Zhang, J. Hofkens, J. A. Steele, M. B. J. Roeffaers, *Angew. Chem., Int. Ed.* **2022**, *61*, e202203261.
- [29] R. Mishra, S. Bera, R. Chatterjee, S. Banerjee, S. Bhattacharya, A. Biswas, S. Mallick, S. Roy, *Appl. Surf. Sci. Adv.* **2022**, *9*, 100241.
- [30] Y. Wu, Q. Wu, Q. Zhang, Z. Lou, K. Liu, Y. Ma, Z. Wang, Z. Zheng, H. Cheng, Y. Liu, Y. Dai, B. Huang, P. Wang, *Energy Environ. Sci.* **2022**, *15*, 1271.
- [31] Y. Wu, P. Wang, X. Zhu, Q. Zhang, Z. Wang, Y. Liu, G. Zou, Y. Dai, M. Whangbo, B. Huang, *Adv. Mater.* **2018**, *30*, 1704342.
- [32] X. Liu, Q. Zhang, S. Zhao, Z. Wang, Y. Liu, Z. Zheng, H. Cheng, Y. Dai, B. Huang, P. Wang, *Adv. Mater.* **2023**, *35*, 2208915.
- [33] J. Yang, D. Wang, H. Han, C. Li, *Acc. Chem. Res.* **2013**, *46*, 1900.
- [34] T. Paul, D. Das, B. K. Das, S. Sarkar, S. Maiti, K. K. Chattopadhyay, *J. Hazard. Mater.* **2019**, *380*, 120855.
- [35] B. Xie, D. Chen, N. Li, Q. Xu, H. Li, J. He, J. Lu, *Chem. Eng. J.* **2022**, *430*, 132968.
- [36] Z.-J. Bai, Y. Mao, B.-H. Wang, L. Chen, S. Tian, B. Hu, Y.-J. Li, C.-T. Au, S.-F. Yin, *Nano Res.* **2022**, *16*, 6104.
- [37] M. Corti, R. Chiara, L. Romani, B. Mannucci, L. Malavasi, P. Quadrelli, *Catal. Sci. Technol.* **2021**, *11*, 2292.
- [38] Y. Wang, H. Huang, Z. Zhang, C. Wang, Y. Yang, Q. Li, D. Xu, *Appl. Catal., B* **2021**, *282*, 119570.
- [39] M. Zhang, W. Wang, F. Gao, D. Luo, *Catalysts* **2021**, *11*, 505.
- [40] M. Medina-Llamas, A. Speltini, A. Profumo, F. Panzarea, A. Milella, F. Fracassi, A. Listorti, L. Malavasi, *Nanomaterials* **2023**, *13*, 263.
- [41] M. Ismael, Y. Wu, *Sustainable Energy Fuels* **2019**, *3*, 2907.
- [42] Z. Guan, Y. Wu, P. Wang, Q. Zhang, Z. Wang, Z. Zheng, Y. Liu, Y. Dai, M.-H. Whangbo, B. Huang, *Appl. Catal., B* **2019**, *245*, 522.
- [43] Q. Huang, Y. Guo, J. Chen, Y. Lou, Y. Zhao, *New J. Chem.* **2022**, *46*, 7395.
- [44] E. T. McClure, M. R. Ball, W. Windl, P. M. Woodward, *Chem. Mater.* **2016**, *28*, 1348.
- [45] X. Wang, K. Maeda, A. Thomas, K. Takanabe, G. Xin, J. M. Carlsson, K. Domen, M. Antonietti, *Nat. Mater.* **2009**, *8*, 76.
- [46] T. Wang, D. Yue, X. Li, Y. Zhao, *Appl. Catal., B* **2020**, *268*, 118399.
- [47] Y. Jiang, K. Li, X. Wu, M. Zhu, H. Zhang, K. Zhang, Y. Wang, K. P. Loh, Y. Shi, Q.-H. Xu, *ACS Appl. Mater. Interfaces* **2021**, *13*, 10037.
- [48] M. Cheng, C. Xiao, Y. Xie, *J. Mater. Chem. A* **2019**, *7*, 19616.
- [49] G. Dong, W. Ho, C. Wang, *J. Mater. Chem. A* **2015**, *3*, 23435.
- [50] Y. Li, M. Ti, D. Zhao, Y. Zhang, L. Wu, Y. He, *J. Alloys Compd.* **2021**, *870*, 159298.
- [51] R. Huang, X. Li, W. Gao, X. Zhang, S. Liang, M. Luo, *RSC Adv.* **2021**, *11*, 14844.
- [52] Y. Zhao, R. Shi, X. Bian, C. Zhou, Y. Zhao, S. Zhang, F. Wu, G. I. N. Waterhouse, L. Wu, C. Tung, T. Zhang, *Adv. Sci.* **2019**, *6*, 1802109.
- [53] A. Sharma, M. Varshney, K. H. Chae, S. O. Won, *Curr. Appl. Phys.* **2018**, *18*, 1458.
- [54] S. Zhang, Y. Yuan, J. Gu, X. Huang, P. Li, K. Yin, Z. Xiao, D. Wang, *Appl. Surf. Sci.* **2023**, *609*, 155446.
- [55] Z. He, Q. Tang, X. Liu, X. Yan, K. Li, D. Yue, *Energy Fuels* **2021**, *35*, 15005.
- [56] J. Xu, J. Liu, B. Liu, J. Wang, B. Huang, *Adv. Funct. Mater.* **2019**, *29*, 1805870.
- [57] M. Palummo, E. Berrios, D. Varsano, G. Giorgi, *ACS Energy Lett.* **2020**, *5*, 457.
- [58] J. Luo, X. Wang, S. Li, J. Liu, Y. Guo, G. Niu, L. Yao, Y. Fu, L. Gao, Q. Dong, C. Zhao, M. Leng, F. Ma, W. Liang, L. Wang, S. Jin, J. Han, L. Zhang, J. Etheridge, J. Wang, Y. Yan, E. H. Sargent, J. Tang, *Nature* **2018**, *563*, 541.
- [59] L. Zhang, Y. Fang, L. Sui, J. Yan, K. Wang, K. Yuan, W. L. Mao, B. Zou, *ACS Energy Lett.* **2019**, *4*, 2975.
- [60] E. Raciti, S. M. Gali, M. Melchionna, G. Filippini, A. Actis, M. Chiesa, M. Bevilacqua, P. Fornasiero, M. Prato, D. Beljonne, R. Lazzaroni, *Chem. Sci.* **2022**, *13*, 9927.
- [61] X. Liu, W. Kang, W. Zeng, Y. Zhang, L. Qi, F. Ling, L. Fang, Q. Chen, M. Zhou, *Appl. Surf. Sci.* **2020**, *499*, 143994.
- [62] P. Huang, M. Grzeszczyk, K. Vaklinova, K. Watanabe, T. Taniguchi, K. S. Novoselov, M. Koperski, *Phys. Rev. B* **2022**, *106*, 014107.
- [63] J. Huang, G. Nie, Y. Ding, *Catalysts* **2019**, *10*, 6.
- [64] A. Speltini, M. Sturini, D. Dondi, E. Annovazzi, F. Maraschi, V. Caratto, A. Profumo, A. Buttafava, *Photochem. Photobiol. Sci.* **2014**, *13*, 1410.
- [65] A. Speltini, L. Romani, D. Dondi, L. Malavasi, A. Profumo, *Catalysts* **2020**, *10*, 1259.
- [66] J. VandeVondele, M. Krack, F. Mohamed, M. Parrinello, T. Chassaing, J. Hutter, *Comput. Phys. Commun.* **2005**, *167*, 103.
- [67] C. Adamo, V. Barone, *J. Chem. Phys.* **1999**, *110*, 6158.
- [68] J. P. Perdew, M. Ernzerhof, K. Burke, *J. Chem. Phys.* **1996**, *105*, 9982.
- [69] S. Grimme, J. Antony, S. Ehrlich, H. Krieg, *J. Chem. Phys.* **2010**, *132*, 154104.
- [70] S. Goedecker, M. Teter, J. Hutter, *Phys. Rev. B* **1996**, *54*, 1703.
- [71] J. VandeVondele, J. Hutter, *J. Chem. Phys.* **2007**, *127*, 114105.
- [72] M. Guidon, J. Hutter, J. VandeVondele, *J. Chem. Theory Comput.* **2010**, *6*, 2348.
- [73] P. Giannozzi, S. Baroni, N. Bonini, M. R. Car, C. Cavazzoni, D. Ceresoli, G. L. Chiarotti, M. Cococcioni, I. Dabo, A. D. Corso, S. de Gironcoli, S. Fabris, G. Fratesi, R. Gebauer, U. Gerstmann, C. Gougoussis, A. Kokalj, M. Lazzeri, L. Martin-Samos, N. Marzari, F. Mauri, R. Mazzarello, S. Paolini, A. Pasquarello, L. Paulatto, C. Sbraccia, S. G. Sciauzero, A. P. Seitsonen, et al., *J. Phys.: Condens. Matter* **2009**, *21*, 395502.
- [74] C. G. Van De Walle, J. Neugebauer, *J. Appl. Phys.* **2004**, *95*, 3851.
- [75] D. Meggiolaro, F. De Angelis, *ACS Energy Lett.* **2018**, *3*, 2206.
- [76] S. Kahmann, D. Meggiolaro, L. Gregori, E. K. Tekelenburg, M. Pitaro, S. D. Stranks, F. De Angelis, M. A. Loi, *ACS Energy Lett.* **2022**, *7*, 4232.
- [77] M. Morana, W. Kaiser, R. Chiara, B. Albin, D. Meggiolaro, E. Mosconi, P. Galinetto, F. De Angelis, L. Malavasi, *J. Phys. Chem. Lett.* **2023**, *14*, 7860.